Journal of Applied Physics

Transport properties of topologically non-trivial bismuth tellurobromides Bi_nTeBr

Cite as: J. Appl. Phys. **126**, 105105 (2019); https://doi.org/10.1063/1.5116369
Submitted: 24 June 2019 . Accepted: 18 August 2019 . Published Online: 09 September 2019

Falk Pabst, Dean Hobbis, Noha Alzahrani, Hsin Wang, I. P. Rusinov, E. V. Chulkov, Joshua Martin, Michael Ruck, and George S. Nolas

AIP Publishing

Journal of Applied Physics ARTICLE scitation.org/journal/jap

Transport properties of topologically non-trivial bismuth tellurobromides Bi_nTeBr

Cite as: J. Appl. Phys. **126**, 105105 (2019); doi: 10.1063/1.5116369
Submitted: 24 June 2019 · Accepted: 18 August 2019 ·
Published Online: 9 September 2019

View Online Export Citation CrossMark

Falk Pabst,[1,2,a)] Dean Hobbis,[2,a)] Noha Alzahrani,[2] Hsin Wang,[3] I. P. Rusinov,[4,5,6] E. V. Chulkov,[5,6,7] Joshua Martin,[8] Michael Ruck,[1,9] and George S. Nolas[2,b)]

AFFILIATIONS

[1]Faculty of Chemistry and Food Chemistry, Technische Universität Dresden, 01062 Dresden, Germany
[2]Department of Physics, University of South Florida, Tampa, Florida 33620, USA
[3]Materials Science and Technology Division, Oak Ridge National Laboratory, 1 Bethel Valley Road, Oak Ridge, Tennessee 37831, USA
[4]Tomsk State University, 634050 Tomsk, Russia
[5]Donostia International Physics Center (DIPC), 20018 Donostia-San Sebastián, Basque Country, Spain
[6]Saint Petersburg State University, 198504 Saint Petersburg, Russia
[7]Departamento de Física de Materiales, UPV/EHU, 20080 Donostia-San Sebastián, Basque Country, Spain
[8]Material Measurement Laboratory, National Institute of Standards and Technology, Gaithersburg, Maryland 20899, USA
[9]Max Planck Institute for Chemical Physics of Solids, Nöthnitzer Str. 40, 01187 Dresden, Germany

Note: This paper is part of the special topic on Advanced Thermoelectrics.
[a)]**Contributions:** F. Pabst and D. Hobbis contributed equally to this paper.
[b)]**Author to whom correspondence should be addressed:** gnolas@usf.edu. **Tel.:** +1-813-974-2233.

ABSTRACT

Temperature-dependent transport properties of the recently discovered layered bismuth-rich tellurobromides Bi_nTeBr (n = 2, 3) are investigated for the first time. Dense homogeneous polycrystalline specimens prepared for different electrical and thermal measurements were synthesized by a ball milling-based process. While the calculated electronic structure classifies Bi_2TeBr as a semimetal with a small electron pocket, its transport properties demonstrate a semiconductorlike behavior. Additional bismuth bilayers in the Bi_3TeBr crystal structure strengthens the interlayer chemical bonding thus leading to metallic conduction. The thermal conductivity of the semiconducting compositions is low, and the electrical properties are sensitive to doping with a factor of four reduction in resistivity observed at room temperature for only 3% Pb doping. Investigation of the thermoelectric properties suggests that optimization for thermoelectrics may depend on particular elemental substitution. The results presented are intended to expand on the research into tellurohalides in order to further advance the fundamental investigation of these materials, as well as investigate their potential for thermoelectric applications.

I. INTRODUCTION

Thermoelectric materials have long been investigated for their potential use in thermoelectric cooling and power generation.[1–3] The suitability of materials for thermoelectricity is defined by the dimensionless figure of merit $ZT = S^2\sigma T/\kappa$, where S is the Seebeck coefficient, σ is the electrical conductivity, T is the absolute temperature, and κ is the thermal conductivity.[1–3] Among many potential materials, bismuth-based compounds are well known for their superior thermoelectric properties.[2] The most prominent representatives belong to bismuth telluride and the structurally related family of group 15 chalcogenides. Different approaches have been investigated to improve the thermoelectric performance of Bi_2Te_3 by tuning the material properties, such as doping or nanoengineering.[2,4–7] Although bismuth tellurides have been extensively studied and the investigation of mixed group 15 tellurides have potential for chemical modification, extending the idea of

chemical diversification further leads to another class of layered bismuth compounds, Bi_nTeX with n = 1–3 and X = Br, I.[8–10]

The bismuth tellurohalides BiTeBr and BiTeI were first reported by Dönges in 1951.[11] Kulbachinskii *et al.*[12] investigated the transport properties of BiTeBr and BiTeI single-crystals, as well as the influence of BiI_3 and CuI doping in polycrystalline BiTeI specimens.[12] Both compounds were reported to be semiconducting with bandgaps of 0.595 and 0.478 eV for BiTeBr and BiTeI, respectively.[12] Wu *et al.*[13] investigated the thermoelectric properties of Cu intercalated BiTeI specimens and mixed halide compounds $BiTeI_{1-x}Br_x$ (x = 0.06, 0.12).[14] The first compound with increased bismuth content in this material system is Bi_2TeI.[8] Subsequently, the bismuth-rich Bi_3TeI and bromine analogs Bi_2TeBr and Bi_3TeBr were synthesized after tribochemical activation of the starting materials by Zeugner *et al.*[9,10] All these compounds are structurally closely related to BiTeX and display the characteristic polar Te-Bi-X triple layer (A) separated by additional bismuth bilayers (B) in the van der Waals gap. Alternate stacking of these two building modules results in either the Bi_2TeX (AAB) or Bi_3TeX (AB) structure types (Fig. 1). Thus far, only the transport properties of Bi_2TeI at and above room temperature have been reported.[15] The bromine counterparts Bi_nTeBr (n = 2, 3) have only recently been reported;[10] thus, their transport properties have not yet been investigated. However, band structure calculations of the bismuth-rich tellurobromides and iodides indicate a complex band structure with band inversion at the Fermi level due to strong spin-orbit coupling.[9,10,16,17] Such an inversion indicates nontrivial band topology that leads to the formation of nontrivial spin-resolved surface states. Murakami *et al.*[18,19] have shown that the interplay of electron conduction in protected conduction channels and phonon transport in the bulk may result in enhanced thermoelectric performance. Here, we report on the transport properties of highly dense polycrystalline specimens of the bromine compounds Bi_3TeBr and Bi_2TeBr, along with Pb-doped and Se-alloyed Bi_2TeBr, in order to build a basis to improve our understanding of this material system in addition to assessing their viability for potential thermoelectric applications.

II. EXPERIMENTAL AND COMPUTATIONAL DETAILS

The synthetic procedure was adopted from that reported previously,[10] and upscaled to multigram products. All chemicals were used as received without further purification.[20] Elemental bismuth (99.997%, Alfa Aesar[20]), tellurium (99.999%, Alfa Aesar), and $BiBr_3$ (99%, Alfa Aesar, stored under an argon atmosphere) were added in stoichiometric amounts along with stainless-steel balls into a stainless-steel chamber (Across International PQN2). The starting materials were ground in the ball mill under an inert gas atmosphere for 6 h at 425 rpm. The tribochemically activated product was subsequently placed in custom-designed stainless-steel tooling lined with graphite foil under a uniaxial pressure of 20 MPa and heated at 623 K for 5 h under a dynamic vacuum of 10^{-6} Torr ($\approx 10^{-4}$ Pa). This system, previously employed for the crystal growth of large complex unit cell structure types,[21–25] allowed for an environment for the rapid formation of the bismuth tellurohalides.

To convert the microcrystalline powders into dense polycrystalline pellets, the specimens were finely ground, sieved (325 mesh), and loaded into a custom-built graphite die and molybdenum punch assembly for hot pressing. Graphite foil was placed between the specimens and the molybdenum punches to prevent reaction with the metal punches. Densification was performed under constant nitrogen flow at 523 K and 160 MPa for 5 h resulting in high-density polycrystalline specimens. Bi_3TeBr was synthesized and densified at 593 K and 513 K, respectively. The structure was characterized by powder X-ray diffraction (PXRD) carried out on a Bruker D8 Focus instrument in Bragg-Brentano geometry with Cu-K_α radiation (1.54 Å, 40 kV, 40 mA) and a graphite monochromator. Analysis of homogeneity was performed by the Rietveld method using the TOPAS software.[26]

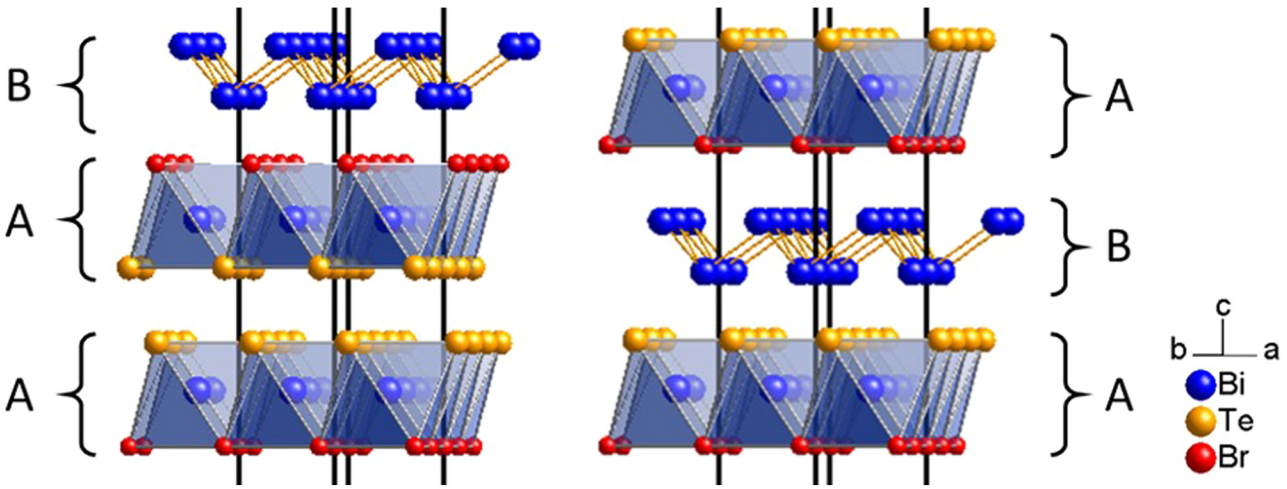

FIG. 1. Section of the unit cell of Bi_nTeBr compounds illustrating AAB and AB stacking of bismuth bilayers and Br-Bi-Te triple layers for Bi_2TeBr (left) and Bi_3TeBr (right).

For transport property measurements the densified pellets were cut with a wire saw. A $2 \times 2 \times 5\ mm^3$ parallelepiped was cut for simultaneous low-temperature (12 K–300 K) four-probe gradient sweep resistivity, ρ, and S measurements performed on a custom-built radiation-shielded vacuum probe.[27] Temperature-dependent κ measurements below room temperature employed the steady state technique in a diffusion-pumped probe with the temperature gradient provided by a chip heater.[28] The maximum experimental uncertainties for these measurements are 7% for ρ, 6% for S, and 8% for κ measurements. High temperature (300–450 K) four-probe ρ and S measurements on a $2 \times 2 \times 10\ mm^3$ parallelepiped were carried out under −0.09 MPa static He in a ULVAC ZEM-3 system with experimental uncertainty between 5% and 8%. Thermal diffusivity, d, was measured by the laser flash method on a NETZSCH LFA 457 system under constant argon flow with an experimental uncertainty of 5%. Thermal conductivity could then be calculated according to $\kappa = DdC_p$. The measurement was performed on a thin disk (diameter = 12.7 mm; height = 2.0 mm) parallel to the pressing axis. Isobaric heat capacity measurements were performed using a Quantum Design Physical Property Measurement System (PPMS) from 2 K to 300 K. The expanded experimental uncertainty ($2u$, where u is the measurement uncertainty and $k = 2$) for the measurement is 1.5%. The density, D, was determined from specimen mass and geometry. The same PPMS system was employed for four-probe temperature-dependent Hall measurements using the AC transport option on $0.5 \times 2.5 \times 6\ mm^3$ parallelepipeds and employing bipolar fields in order to reduce voltage probe misalignment effects, with an experimental uncertainty ($2u$) of 5%.

In calculating transport and thermoelectric properties of Bi_2TeBr, the Boltzwann code,[29] as a part of the WANNIER90[30] package, was employed. The relaxation time was chosen to be 10 fs, and the dense mesh was set to $300 \times 300 \times 300$ (k-points). This grid density was sufficient to consider the thermoelectric quantities at a temperature of 50 K. The bases of the Wannier functions were p_x, p_y, and p_z for each atom of the unit cell and spinor component. The OPENMX DFT code[31] was used to obtain an electronic structure within DFT for subsequent Wannier interpolation. The basis of pseudoatomic orbitals was chosen to be s2p2d2f1 for each type of atomic species.[32] The exchange-correlation energy was treated using the generalized gradient approximation.[33] The Hamiltonian contained scalar relativistic corrections, with spin-orbit coupling taken into account by the second variation method.[34]

III. RESULTS AND DISCUSSION

PXRD and Rietveld refinement indicated a small BiOBr impurity in the Bi_2TeBr specimens (Fig. S1 in the supplementary material) and a larger amount in Bi_3TeBr (Fig. S2). $BiBr_3$ is very sensitive to ambient moisture and easily forms the oxide; thus, BiOBr formation could not be entirely eliminated from the multi-step process. For the lead doped specimen, very low intensity diffraction peaks identified as $PbBr_2$ were also present. Based on our refinement results, the incorporated lead concentration in Bi_2TeBr was 3% ($Bi_{1.94}Pb_{0.06}TeBr$). Doping on the tellurium position with selenium did not result in any Se-containing side phases. Both $PbBr_2$ and BiOBr are large bandgap materials and will therefore not have a significant influence on the physical properties presented here. The Bi_3TeBr specimen also contained trace amounts of Bi_2Te_3 (Fig. S2 in the supplementary material).

The temperature-dependent electrical ρ and S values are shown in Fig. 2. Bi_2TeBr displays a semiconductor behavior with ρ decreasing with increasing temperature. The room temperature ρ values of the lead and selenium doped specimens were reduced by more than a factor of two compared to that of undoped Bi_2TeBr and over a factor of four at lower temperatures. As shown in Fig. 2(a), both specimens display a weak temperature-dependent increase of ρ with decreasing temperature, indicating an increase in conductivity with doping, whereas the Bi_3TeBr specimen shows metallic temperature dependence. The difference in ρ values is reflected in the S data shown in Fig. 2(b) with the S values for the lead and selenium doped specimens being smaller than that of the undoped Bi_2TeBr specimen in the entire measured temperature range. The temperature-dependent S data allow for an estimate of the bandgap employing $S_{max} = E_g/2eT_{max}$, where E_g is the bandgap, e is the charge of the electron, and T_{max} is the temperature corresponding to the maximum S value.[35] Using this approach, we estimate E_g for the three semiconducting specimens to be between 0.05 and 0.08 eV. This is in good agreement with the estimated gap for Bi_2TeBr based on a linear fit of the high temperature ρ data, $\rho = \rho_0 \exp(E_g/2k_BT)$, where k_B is the Boltzmann constant (Figs. S3, S4, and S5 in the supplementary material), and

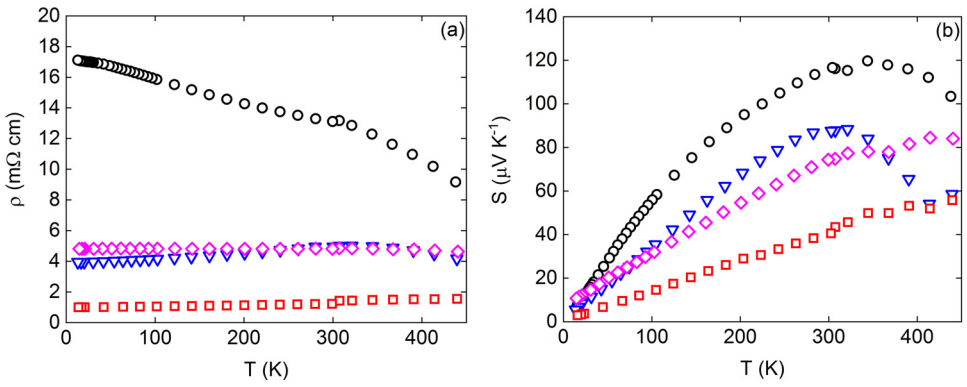

FIG. 2. Temperature-dependent (a) ρ and (b) S for Bi_2TeBr (○), $Bi_{1.8}Pb_{0.2}TeBr$ (▽), $Bi_2Se_{0.3}Te_{0.7}Br$ (◇), and Bi_3TeBr (□).

also corresponds well with the global bandgap for Bi_2TeBr from DFT calculations.[10]

The S values for the three Bi_2TeBr specimens are significantly larger than that reported for Bi_2TeI, with S_{max} being twice as high for Bi_2TeBr than that for Bi_2TeI.[15] In contrast to the bismuth-poor materials,[36] Fig. 2(b) indicates positive S values for Bi_2TeBr and Bi_3TeBr. The interaction between bismuth bilayers stacked in between the polar Te-Bi-Br layer seems to have a significant impact on the electrical properties. Specifically, stronger intralayer interactions and higher delocalization are introduced by increasing the number of Bi bilayers, resulting in a more metallic character of the electronic structure.[10] This tendency manifests itself stronger for a higher Bi to TeBiBr ratio and is corroborated by our experimental data.

The temperature-dependent mobility, μ, from Hall data is shown in Fig. 3. All four specimens' trend toward a $T^{3/2}$ dependence near room temperature indicative of charge carrier scattering primarily by lattice phonons above room temperature. Room temperature hole concentrations for $Bi_{1.8}Pb_{0.2}TeBr$ and $Bi_2Se_{0.3}Te_{0.7}Br$ are 1.2×10^{20} cm^{-3} and 5.8×10^{20} cm^{-3}, respectively. Of particular note is the fact that Bi_2TeBr is characterized by a positive S and negative Hall conductivity (room temperature electron concentration of 1.4×10^{20} cm^{-3}). This behavior can be explained by *ab initio* calculations of the electronic structure within DFT and our transport measurements. The calculated density of states (DOS) [Fig. 4(a)] shows a nearly semiconducting character of electronic structure with a vanishingly small value at the Fermi level that is caused by a small hole pocket, as reported in the previous DFT study of this compound.[10] Another prominent feature is a DOS minimum at 0.6 eV. As we describe below, both these features are key to understanding the behavior of transport properties and charge doping for Bi_2TeBr.

In Fig. 4(b) the temperature dependence of the spatially averaged electric resistivity [$\rho = (\rho_{xx}+\rho_{yy}+\rho_{zz})/3$] with respect to E-E_F is presented. The behavior of this quantity is in qualitative agreement with our experimental data, as well as with the DOS calculations, suggesting a semiconducting-type conductivity for Bi_2TeBr. The energy dependence shows an increase in the electrical conductivity, σ, with charge doping due to the shift in chemical potential, as reflected in the sharp peak (50 mΩ cm at 50 K) of ρ at the Fermi level. In addition, a decrease in ρ with increasing T is observed. There is an additional peak in ρ at 0.6 eV that implies a reduction in conductivity at a given electron concentration. The peak maximum is 3 mΩ cm at 450 K and monotonically increases with increasing T up to 5 mΩ cm at 50 K. These values are smaller than that at the Fermi level suggesting a semimetallic or weak metallic character at this energy. In this way, according to the calculated DOS and ρ, two energy areas appear where Bi_2TeBr manifests nonmetallic properties, at the Fermi level and at 0.6 eV above E_F.

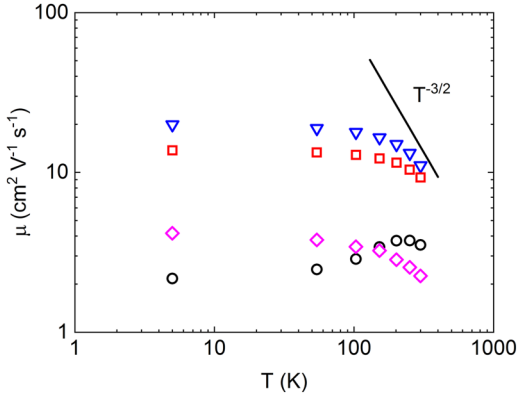

FIG. 3. Temperature-dependent mobility for Bi_2TeBr (○), $Bi_{1.8}Pb_{0.2}TeBr$ (▽), $Bi_2Se_{0.3}Te_{0.7}Br$ (◇), and Bi_3TeBr (□). The $\mu \sim T^{-3/2}$ behavior expected from acoustic phonon scattering of charge carriers is illustrated by a solid line near room temperature.

Bi_2TeBr is characterized by strong crystal anisotropy. Two building blocks (bismuth bilayers and BiTeBr trilayers) are separated by van der Waals spacing along the preferential z-direction; therefore, the calculated transport quantities are distinguished for different directions. In Fig. 4(c), ρ_{xx} and ρ_{zz} are shown at 300 K. As is clear from this figure, ρ_{zz} is significantly larger than ρ_{xx} due to the weak chemical interaction between the building blocks. Also, in contrast to ρ and ρ_{xx}, ρ_{zz} is characterized by additional peaks at −0.9 eV, −0.4 eV, and 1.0 eV. The positions of these peaks are related to the DOS gradient shown in Fig. 4(a).

The existence of these two peculiarities in ρ and DOS for Bi_2TeBr is reflected in our calculated S values. Spatially averaged $S = (S_{xx}+S_{yy}+S_{zz})/3$ is presented in Fig. 4(d). Similar to ρ, two sharp features related to a change of sign for S are observed, denoted by blue and green shaded areas. Each feature forms two peak structures with an opposite sign to that of the peaks. The quantity is strongly dependent on the temperature: the increase of T up to T_{max} leads to an increase in the absolute value of the peak maxima. Near the Fermi level, both the positive and negative peaks have T_{max} equal to 200 K and 450 K at 0.6 eV and 300 K, respectively. Our experimentally measured positive S and n-type Hall data can be explained by shifting the chemical potential to the area of the positive peak at 0.6 eV. This is also in accordance with the slightly larger experimental T_{max} at 350 K [see Fig. 2(b)]. The existence of a two-peak feature at 0.6 eV is evidence of the strong influence of charge doping on the thermoelectric properties. The crystal anisotropy also leads to a difference between S_{xx} and S_{zz} [Fig. 4(e)]. The out-of-plane S demonstrates most prominently this difference in comparison to S_{xx}. Near the Fermi level, the absolute value of S_{zz} is slightly smaller than that for S_{xx}; however, outside of this region, S_{zz} is larger particularly in the areas near −0.6 eV, −0.3 eV, and 1 eV.

The calculated Hall conductivity, σ_{xy} [Fig. 4(f)], for Bi_2TeBr is negative for n-type doping and forms two broad extrema at 0.4 eV and 0.8 eV. The positions of the extrema are associated with large values of the DOS [see also Fig. 4(a)]. The temperature dependence of σ is only affected by smearing effects. The result of our theoretical calculations agrees with the measurements and confirms the shift of the chemical potential at 0.6 eV.

Our electronic structure calculations and transport property measurements indicate a metallic character for Bi_3TeBr, in full agreement with the previous *ab initio* simulations.[10] As shown in

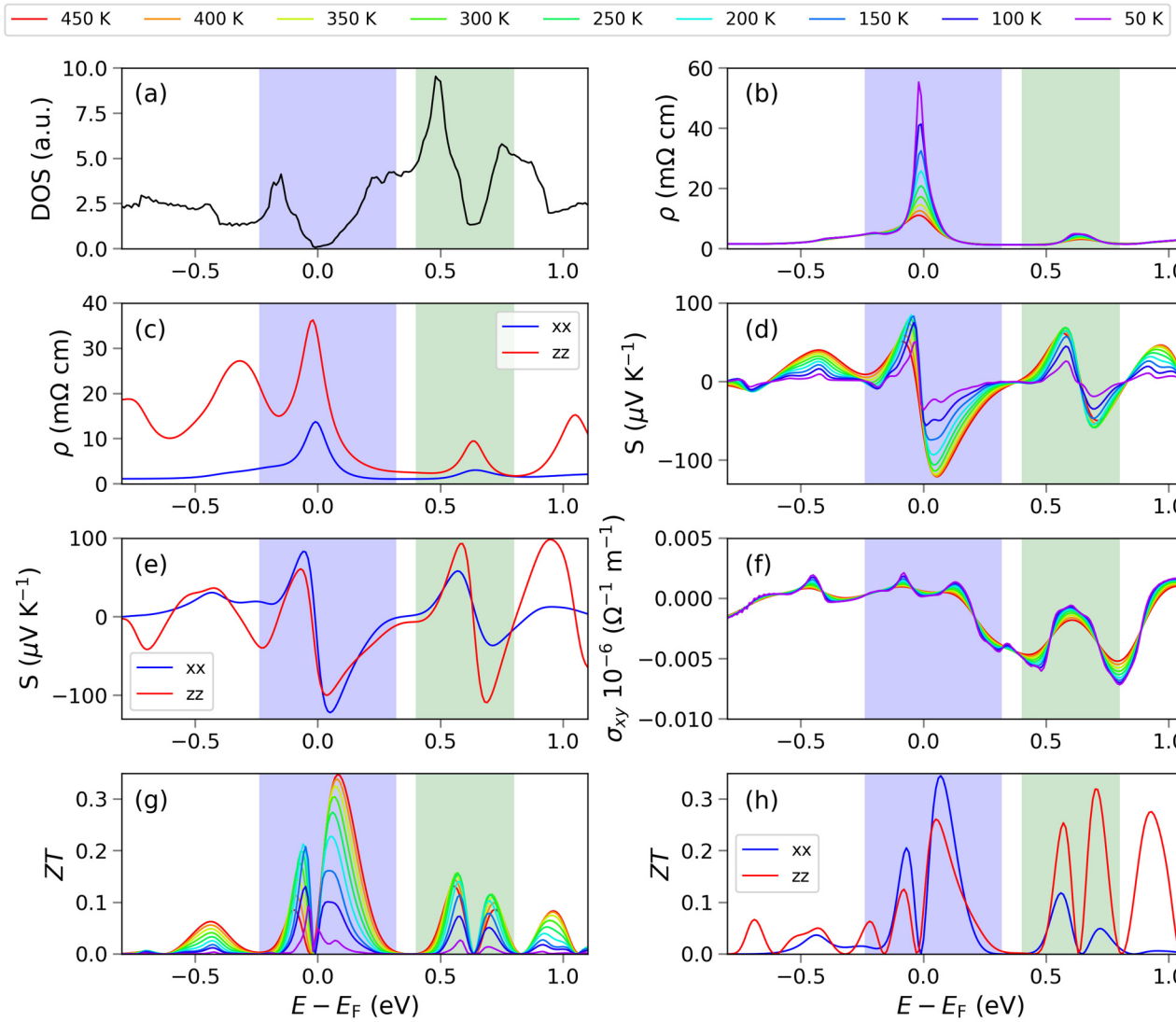

FIG. 4. Calculated (a) density of states (DOS), (b) spatially averaged resistivity, ρ, (c) ρ_{xx} and ρ_{zz} at 300 K (blue and red curves, respectively), (d) spatially averaged S, (e) S_{xx} and S_{zz} at 300 K (blue and red curves, respectively), (f) Hall conductivity, (g) spatially averaged ZT, and (h) in-plane (xx) and out-of-plane (zz) components of ZT at 300 K (blue and red curves, respectively) for Bi_2TeBr. For (b), (d), (f), and (g), all quantities are presented for a temperature range of 50 K (violet color) to 450 K (red color). The blue and green background colors represent two areas of high thermoelectric performance (as described in the text).

Fig. 5, the DOS plot has two minima, at the Fermi level and at E-E_F = 0.9 eV, although the DOS values are in general larger than for Bi_2TeBr [Fig. 4(a)]. In agreement with the nonmetallic behavior, the transport properties for Bi_2TeBr [Figs. 4(b)–4(e)] show a slightly decreasing conductivity and temperature-dependent resistivity near the Fermi level where the smaller minimum of the DOS is localized. This is indicated by a shallow peak in ρ for this energy range. The smaller value of ρ for Bi_3TeBr, as well as the weak temperature dependence for ρ, agrees with the experimental results [Fig. 2(a)]. Two peaklike peculiarities are also observed in the energy dispersions of S and ZT at the Fermi level and at E-E_F = 0.9 eV.

The Bi_2TeBr specimens display low κ values in the measured temperature range (Fig. 6), comparable to that of Bi_2Te_3 as well as other low κ materials.[2,37] Temperature-dependent C_P for Bi_2TeBr is shown in Fig. 7. The inset shows C_P/T vs T^2 for the low-temperature (1.8 K < T < 3.1 K) data along with a simple linear fit of the form $C_P/T = \beta T^2 + \gamma$, where the β coefficient relates the lattice contribution and γ, the Sommerfeld coefficient, is the electronic contribution to the specific heat. Our fit results in $\beta = 3.6\ \mathrm{mJ\ mol^{-1}\ K^{-4}}$ and

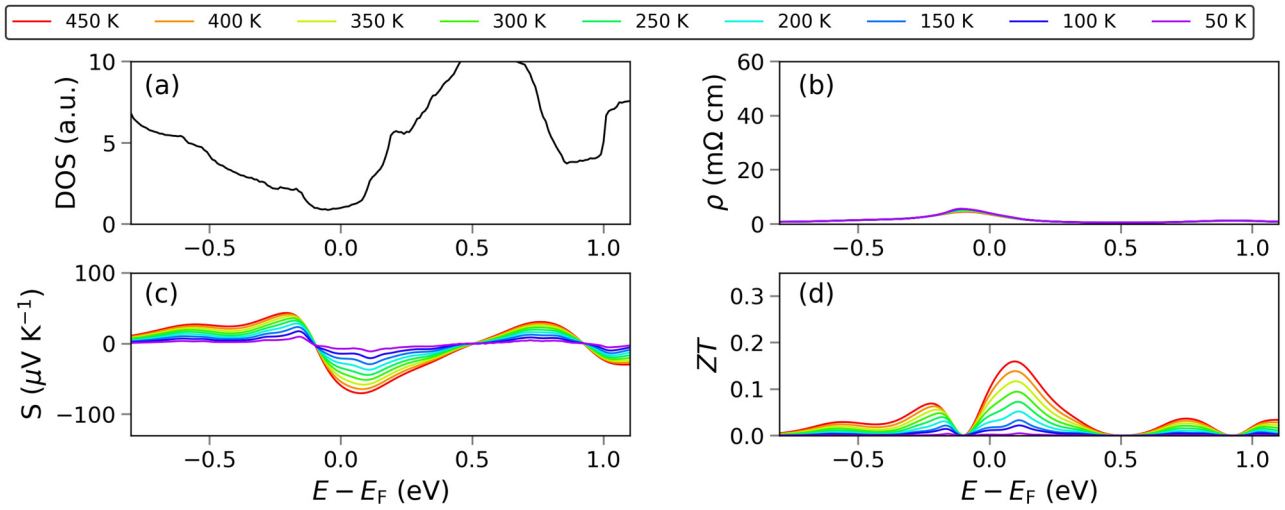

FIG. 5. Calculated (a) DOS, (b) spatially averaged ρ, (c) S, and (d) ZT for Bi_3TeBr. All quantities are presented for a temperature range of 50 K (violet color) to 450 K (red color).

$\gamma = 0.06$ mJ mol^{-1} K^{-2} for Bi_2TeBr. Very similar values were obtained from C_P data of the Pb-doped and Se-alloyed specimens (Figs. S6 and S7 in the supplementary material). The same method for Bi_3TeBr results in $\beta = 4.9$ mJ mol^{-1} K^{-4} and $\gamma = 0.32$ mJ mol^{-1} K^{-2} (Fig. S8 in the supplementary material), values that are similar to that for Bi_2Te_3 while γ is about half the value of Cu.[38,39] The β value obtained for the Bi_2TeBr specimens are larger than that reported for $CuSbS_2$, which displays very low κ values.[40] Using the values of β obtained from our low-temperature fits to the C_P data for all four specimens, one can estimate the Debye temperature, θ_D, from[41]

$$\theta_D = \left(\frac{12\pi^4 R n_a}{5\beta}\right)^{1/3}, \quad (1)$$

where R is the molar gas constant and n_a is the number of atoms per unit cell. This results in values of 235 K for all three Bi_2TeBr specimens and 181 K for Bi_3TeBr. The θ_D value for Bi_3TeBr is similar to that reported for Bi_2Te_3, while θ_D for Bi_2TeBr is larger.[38,39]

Figure 8 shows ZT for all specimens. The maximum value of ZT (ZT_{max}) is similar for both doped specimens, while the selection of the dopant allows for a shift in ZT_{max} to lower (lead) or higher (selenium) temperatures compared to the undoped specimen. Figure 8 indicates that these specimens have low ZT values; nevertheless, our fundamental investigation into the transport

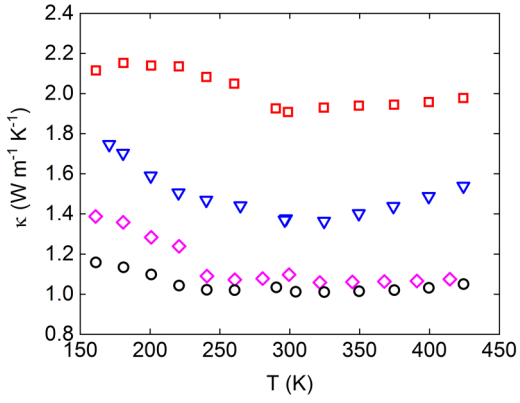

FIG. 6. Temperature-dependent κ for Bi_2TeBr (○), $Bi_{1.8}Pb_{0.2}TeBr$ (▽), $Bi_2Se_{0.3}Te_{0.7}Br$ (◇), and Bi_3TeBr (□).

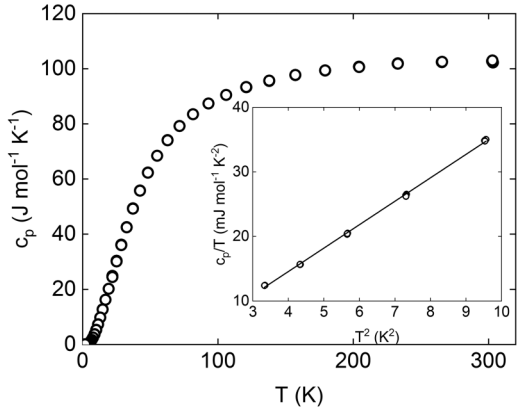

FIG. 7. Temperature-dependent heat capacity shown for Bi_2TeBr (○), with data for the other compositions shown in Figs. S6–S8 in the supplementary material. The inset shows low-temperature data with a linear fit of the form $C_P/T = \beta T^2 + \gamma$.

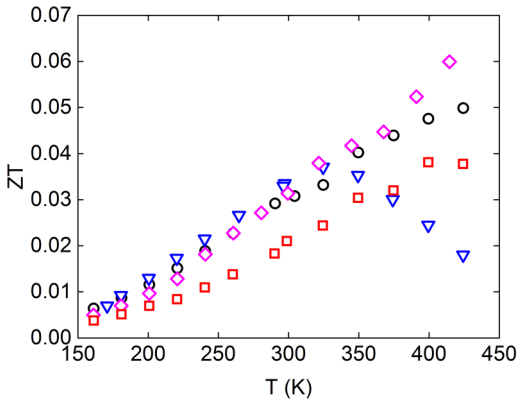

FIG. 8. Temperature-dependent ZT for Bi_2TeBr (○), $Bi_{1.8}Pb_{0.2}TeBr$ (▽), $Bi_2Se_{0.3}Te_{0.7}Br$, (◇) and Bi_3TeBr (□).

properties of pure and doped Bi_2TeBr indicates that the thermoelectric properties may be influenced by the dopant and thus the possibility for further optimization of their thermoelectric properties. To this end, we note the *ZT* values from the calculated *S*, σ, and the electronic part of κ and κ_e, in Figs. 4(g) and 4(h). The sequence of maxima observed for *ZT* arise at the same energies as that for *S*. The *ZT* curve is characterized by a sequence of peaks formed at the same energy as for the *S* curve, as seen in Fig. 4(d). For each peak, the maximum of *ZT* increases together with *T* up to T_{max}. The values of T_{max} for each *ZT* peak are the same as that for *S*. The highest peak is located near the Fermi level at 0.1 eV and corresponds to a *ZT* of 0.35. At $E\text{-}E_F > -0.5$ eV, the peaks for the out-of-plane *ZT* are much larger in comparison with that of the in-plane values [Fig. 4(h)].

Figure 9(a) shows a schematic illustrating the differing electronic and transport properties of Bi_nTeBr. Whereas BiTeBr and Bi_3TeBr exhibit purely semiconducting and metallic behavior, respectively, Bi_2TeBr lies on the borderline between a semimetal and a semiconductor phase. The transport properties of Bi_2TeBr are characterized by two main features, spatial anisotropy and alternation at charge doping, which can be explained by the band structure of this material. The band spectrum of Bi_2TeBr calculated along the high-symmetry lines is shown in Fig. 9(b). Its semimetallic, nearly semiconducting, behavior is clear. The edges of the global bandgap (the blue colored area) form a number of valleys with a complex dispersion that defines the transport and thermoelectric properties near the Fermi level as well as the high value of ρ and the peaks in *S* and *ZT*. A weak van der Waals interaction between the building blocks of Bi_2TeBr enhances the quasi-two-dimensional character of the band structure. As a result, two unoccupied bands form a local gap (the green colored area) and sharp minima in DOS at 0.6 eV, as reflected by the peculiarities in the transport properties. A similar behavior has been reported in two-dimensional materials such as SnS[42] and phosphorene[43] nanoribbons. These computations displaying the complex transport in Bi_2TeBr, in addition to the sensitivity of the electrical properties to the doping level, as well as the low κ values reported here, suggest that additional research into this material system are of interest for potential thermoelectric applications.

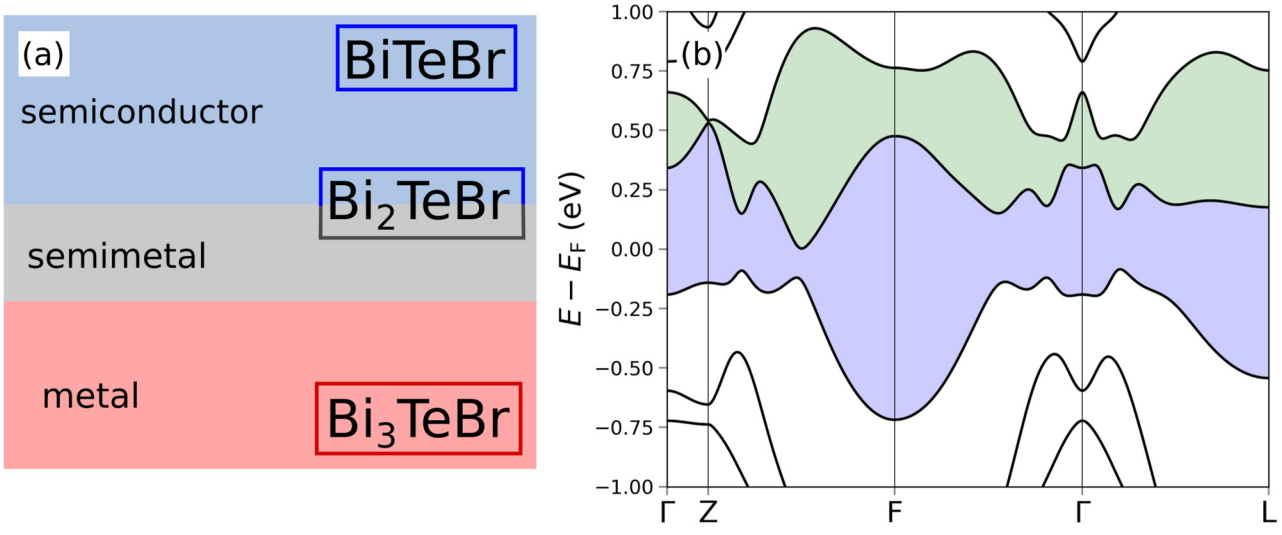

FIG. 9. (a) Schematic illustrating the different electronic phases for the Bi_nTeBr compositions. (b) Electronic structure along the high-symmetry points in Bi_2TeBr. The blue and green background colors represent the regions centered at the Fermi level and at $E\text{-}E_F = 0.6$ eV, respectively. The regions are formed by bands that are the source of high thermoelectric performance (note also Fig. 4).

IV. CONCLUSION

Electrical and thermal transport properties of undoped and doped Bi_2TeBr, as well as the bismuth-rich compound Bi_3TeBr, are reported for the first time. The impact of doping on these materials has been demonstrated with a significant reduction in ρ for $Bi_{1.94}Pb_{0.06}TeBr$ and $Bi_2Te_{0.7}Se_{0.3}Br$ as compared to Bi_2TeBr. Bi_2TeBr also displays relatively large S values, twice as high as those reported for the iodine analog. In addition, there is potential to tailor the transport properties of this material system, demonstrated by the fact that the choice of dopant allows for tunability of the transport properties. Furthermore, Bi_2TeBr shows nontrivial transport due to its quasi-two-dimensional character and peculiarities in the DOS. A shift from semimetallic to metallic behavior was observed by adding additional bismuth bilayers (Fig. 1). The measured ZT values are much smaller than that of the state-of-the-art bismuth telluride-based compounds;[2] however, our work has shown that these materials are of interest for further investigation, as newly discovered potential topological insulators possess interesting transport properties in the search for new thermoelectric materials.

SUPPLEMENTARY MATERIAL

Powder X-ray diffraction, temperature-dependent $\mathrm{Ln}(\rho)$ data for Bi_2TeBr, $Bi_{1.8}Pb_{0.2}TeBr$, and $Bi_2Se_{0.3}Te_{0.7}Br$ with a solid line fit of the form $\rho = \rho_0 \exp(E_g/2k_BT)$, and temperature-dependent C_P for $Bi_{1.8}Pb_{0.2}TeBr$, $Bi_2Se_{0.3}Te_{0.7}Br$, and Bi_3TeBr are shown in the supplementary material.

ACKNOWLEDGMENTS

The authors acknowledge Dr. Anna Isaeva for fruitful discussions and suggestions. This work was supported by the ERASMUS+ ICM WORLDWIDE exchange program funded by the European Union. F.P. and M.R. acknowledge financial support from the Deutsche Forschungsgemeinschaft (DFG) through the Würzburg-Dresden Cluster of Excellence on Complexity and Topology in Quantum Matter—ct.qmat (EXC 2147, Project No. 39085490). G.S.N. acknowledges the support from the U.S. National Science Foundation (NSF) under Grant No. DMR-1748188. D.H. acknowledges the II-VI Foundation Block-Gift Program. H.W. acknowledges the support of the assistant secretary of Energy Efficiency and Renewable Energy and the Materials Program under the Vehicle Technologies Program. Oak Ridge National Laboratory is managed by UT-Batelle LLC under Contract No. DE-AC05000OR22725. I.P.R. acknowledges the support from the Ministry of Education and Science of the Russian Federation within the framework of the governmental program "Megagrants" (State Task No. 3.8895.2017/P220) (for theoretical investigation of thermoelectric properties of Bi_3TeBr), Academic D. I. Mendeleev Fund Program of Tomsk State University (Project No. 8.1.01.2018), and by the Russian Science Foundation No. 18-12-00169 (for theoretical investigation of thermoelectric properties of Bi_2TeBr); E.V.C. and I.P.R. also acknowledge the support from Saint Petersburg State University (Project No. 15.61.202.2015).

REFERENCES

[1]S. LeBlanc, Sustain. Mater. Technol. **1–2**, 26 (2014).
[2]G. S. Nolas, J. Sharp, and J. Goldsmid, *Thermoelectrics: Basic Principles and New Materials* (Springer-Verlag, 2001).
[3]L. E. Bell, Science **321**, 1457 (2008).
[4]D. Kusano and Y. Hori, J. Jpn. Inst. Met. **66**, 1063 (2002).
[5]H.-J. Wu and W.-T. Yen, Acta Mater. **157**, 33 (2018).
[6]M. Takashiri, K. Miyazaki, S. Tanaka, J. Kurosaki, D. Nagai, and H. Tsukamoto, J. Appl. Phys. **104**, 084302 (2008).
[7]S.-S. Lin and C.-N. Liao, J. Appl. Phys. **110**, 093707 (2011).
[8]S. V. Savilov, V. N. Khrustalev, A. N. Kuznetsov, B. A. Popovkin, and M. Yu. Antipin, Russ. Chem. Bull. **54**, 87 (2005).
[9]A. Zeugner, M. Kaiser, P. Schmidt, T. V. Menshchikova, I. P. Rusinov, A. V. Markelov, W. Van den Broek, E. V. Chulkov, T. Doert, M. Ruck, and A. Isaeva, Chem. Mater. **29**, 1321 (2017).
[10]A. Zeugner, J. Teichert, M. Kaiser, T. V. Menshchikova, I. P. Rusinov, A. V. Markelov, E. V. Chulkov, T. Doert, M. Ruck, and A. Isaeva, Chem. Mater. **30**, 5272 (2018).
[11]E. Dönges, Z. Anorg. Allg. Chem. **265**, 56 (1951).
[12]V. A. Kulbachinskii, V. G. Kytin, A. A. Kudryashov, A. N. Kuznetsov, and A. V. Shevelkov, J. Solid State Chem. **193**, 154 (2012).
[13]L. Wu, J. Yang, M. Chi, S. Wang, P. Wei, W. Zhang, L. Chen, and J. Yang, Sci. Rep. **5**, 14319 (2015).
[14]L. Wu, J. Yang, T. Zhang, S. Wang, P. Wei, W. Zhang, L. Chen, and J. Yang, J. Phys. Condens. Matter **28**, 085801 (2016).
[15]K. Tu, P. Wei, H. Zhou, X. Mu, W. Zhu, X. Nie, and W. Zhao, Energies **11**, 891 (2018).
[16]P. Tang, B. Yan, W. Cao, S.-C. Wu, C. Felser, and W. Duan, Phys. Rev. B **89**, 041409 (2014).
[17]I. P. Rusinov, T. V. Menshchikova, A. Isaeva, S. V. Eremeev, Yu. M. Koroteev, M. G. Vergniory, P. M. Echenique, and E. V. Chulkov, Sci. Rep. **6**, 20734 (2016).
[18]S. Murakami, R. Takahashi, O. A. Tretiakov, A. Abanov, and J. Sinova, J. Phys. Conf. Ser. **334**, 012013 (2011).
[19]R. Takahashi and S. Murakami, Semicond. Sci. Technol. **27**, 124005 (2012).
[20]Certain commercial equipment instrumentation or materials are identified in this document. Such identification does not imply recommendation or endorsement by the National Institute of Standards and Technology, nor does it imply that the products identified are the best available for the purpose.
[21]S. Stefanoski, J. Martin, and G. S. Nolas, J. Phys. Condens. Matter **22**, 485404 (2010).
[22]S. Stefanoski, M. Beekman, W. Wong-Ng, P. Zavalij, and G. S. Nolas, Chem. Mater. **23**, 1491 (2011).
[23]S. Stefanoski and G. S. Nolas, Cryst. Growth Des. **11**, 4533 (2011).
[24]S. Stefanoski, C. D. Malliakas, M. G. Kanatzidis, and G. S. Nolas, Inorg. Chem. **51**, 8686 (2012).
[25]Y. Dong, P. Chai, M. Beekman, X. Zeng, T. M. Tritt, and G. S. Nolas, Inorg. Chem. **54**, 5316 (2015).
[26]R. W. Cheary and A. Coelho, J. Appl. Crystallogr. **25**, 109 (1992).
[27]J. Martin, S. Erickson, G. S. Nolas, P. Alboni, T. M. Tritt, and J. Yang, J. Appl. Phys. **99**, 044903 (2006).
[28]J. Martin and G. S. Nolas, Rev. Sci. Instrum. **87**, 015105 (2016).
[29]G. Pizzi, D. Volja, B. Kozinsky, M. Fornari, and N. Marzari, Comput. Phys. Commun. **185**, 422 (2014).
[30]A. A. Mostofi, J. R. Yates, G. Pizzi, Y.-S. Lee, I. Souza, D. Vanderbilt, and N. Marzari, Comput. Phys. Commun. **185**, 2309 (2014).
[31]T. Ozaki, Phys. Rev. B **67**, 155108 (2003).
[32]T. Ozaki and H. Kino, Phys. Rev. B **69**, 195113 (2004).
[33]J. P. Perdew, K. Burke, and M. Ernzerhof, Phys. Rev. Lett. **78**, 1396 (1997).
[34]D. D. Koelling and B. N. Harmon, J. Phys. C Solid State Phys. **10**, 3107 (1977).
[35]H. J. Goldsmid and J. W. Sharp, J. Electron. Mater. **28**, 869 (1999).
[36]J.-Z. Xin, C.-G. Fu, W.-J. Shi, G.-W. Li, G. Auffermann, Y.-P. Qi, T.-J. Zhu, X.-B. Zhao, and C. Felser, Rare Metals **37**, 274 (2018).

[37]D. G. Cahill and R. O. Pohl, Phys. Rev. **35**, 4067 (1987).
[38]G. E. Shoemake, J. A. Rayne, and R. W. Ure, Jr., Phys. Rev. **185**, 1046 (1969).
[39]E. S. Itskevich, Sov. Phys. JETP **11**, 255 (1960).
[40]D. Hobbis, K. Wei, H. Wang, J. Martin, and G. S. Nolas, Inorg. Chem. **56**, 14040 (2017).
[41]C. Kittel, *Introduction to Solid State Physics* (John Wiley & Sons, 1996).
[42]L. M. Sandonas, D. Teich, R. Guitierrez, T. Lorenz, A. Pecchia, G. Seifert, and G. Cunibert, J. Phys. Chem. C **120**, 18841 (2016).
[43]J. Zhang, H. J. Liuy, L. Cheng, J. Wei, J. H. Liang, D. D. Fan, J. Shi, X. F. Tang, and Q. J. Zhang, Sci. Rep. **4**, 6452 (2014).